FIRST ACETIC ACID SURVEY WITH CARMA IN HOT MOLECULAR CORES

Y.-S. JERRY SHIAO[1,2], LESLIE W. LOONEY[1], ANTHONY J. REMIJAN[3,4], LEWIS E. SNYDER[1], and DOUGLAS N. FRIEDEL[1]

ABSTRACT

Acetic acid (CH_3COOH) has been detected mainly in hot molecular cores where the distribution between oxygen (O) and nitrogen (N) containing molecular species is co-spatial within the telescope beam. Previous work has presumed that similar cores with co-spatial O and N species may be an indicator for detecting acetic acid. However, does this presumption hold as higher spatial resolution observations become available of large O and N-containing molecules? As the number of detected acetic acid sources is still low, more observations are needed to support this postulate. In this paper, we report the first acetic acid survey conducted with the Combined Array for Research in Millimeter-wave Astronomy (CARMA) at 3 mm wavelengths towards G19.61-0.23, G29.96-0.02 and IRAS 16293-2422. We have successfully detected CH_3COOH via two transitions toward G19.61-0.23 and tentatively confirmed the detection toward IRAS 16293-2422 A. The determined column density of CH_3COOH is $2.0(1.0)\times10^{16}$ cm^{-2} and the abundance ratio of CH_3COOH to methyl formate ($HCOOCH_3$) is $2.2(0.1)\times10^{-1}$ toward G19.61-0.23. Toward IRAS 16293 A, the determined column density of CH_3COOH is $\sim1.6\times10^{15}$ cm^{-2} and the abundance ratio of CH_3COOH to methyl formate ($HCOOCH_3$) is $\sim1.0\times10^{-1}$ both of which are consistent with abundance ratios determined toward other hot cores. Finally, we model all known line emission in our passband to determine physical conditions in the regions and introduce a new metric to better reveal weak spectral features that are blended with stronger lines or that may be near the 1-2σ detection limit.

Subject headings: ISM: abundances — ISM: individual (G19.61-0.23, G29.96-0.02, IRAS 16293-2422) — ISM: molecules — ISM: clouds

[1]Department of Astronomy, University of Illinois at Urbana-Champaign, Urbana, IL 61801, USA

[2]Physics Department, National Taiwan University, Taipei 10617, Taiwan; jshiao@phys.ntu.edu.tw

[3]National Radio Astronomy Observatory, Charlottesville, VA 2290, USA; aremijan@nrao.edu

[4]Center for Chemistry of the Universe, Department of Chemistry, University of Virginia, McCormack Rd., P.O. Box 400319, Charlottesville, VA 22904-4319

1. INTRODUCTION

With high resolution observations, Sgr B2 has been resolved into many regions of compact molecular/continuum emission (Gaume et al. 1995); one of these regions, Sgr B2(N-LMH) (i.e., the "Large Molecule Heimat") (Snyder et al. 1994; Miao et al. 1995), is a molecule-rich hot core that has historically been the best place to search for large and complex molecules. Interstellar acetic acid (CH_3COOH) was first detected in the hot molecular core (HMC) of Sgr B2(N-LMH) with the Berkeley-Illinois-Maryland Association (BIMA) and Owens Valley Radio Observatory (OVRO) millimeter-wavelength arrays by Mehringer et al. (1997). The compactness of the CH_3COOH emission in Sgr B2(N-LMH) ($<3''$) (e.g., Remijan et al. 2002) highlights the importance of interferometers. To clearly detect the compact emission features from CH_3COOH and other large molecules toward hot cores embedded in regions of more extended molecular emission, high resolution interferometric observations are necessary. Thus, following the first CH_3COOH detections in Sgr B2(N-LMH) and using the BIMA array, Remijan et al. (2002) confirmed CH_3COOH in Sgr B2(N-LMH) and discovered the second CH_3COOH source, the hot core toward W51e2.

Remijan et al. (2003) launched an extensive CH_3COOH survey of 12 galactic HMCs, including high-mass (≥ 10 $M_\odot$) and low-mass (< 10 $M_\odot$) sources, and they found the third CH_3COOH source toward the high-mass HMC G34.3+0.15. Using the IRAM 30-m telescope, Cazaux et al. (2003) reported the first detection of CH_3COOH in IRAS 16293-2422 via the $9_{*,9} - 8_{*,8}$ E line at 100.855 GHz. This is the first low-mass star forming region with detected CH_3COOH to date, making only a total of four known interstellar sources of CH_3COOH. At the conclusion of the search for new sources of CH_3COOH, it was found that the three high mass regions containing CH_3COOH emission share certain chemical properties. For example, the abundances of CH_3COOH and its isomer methyl formate ($HCOOCH_3$) are very different; in Sgr B2(N-LMH), the abundance of $HCOOCH_3$ is 26 times higher than that of CH_3COOH (Snyder 2006) assuming the emission from CH_3COOH and $HCOOCH_3$ are co-spatial within the telescope beam. In addition, it has been suggested by Remijan et al. (2004) that there is a relationship between the CH_3COOH sources and the spatial separation of complex oxygen (O) (e.g. $HCOOCH_3$ and CH_3COCH_3) and nitrogen (N) containing species (e.g. CH_3CH_2CN and NH_2CH_2CN). At the limit of the current observational resolution of these surveys, CH_3COOH emission is only detected where the emission from O and N-containing species is co-spatial. In contrast, there have not been any CH_3COOH detections in HMCs with reported spatial separation of complex O and N-containing species, e.g. Orion KL (e.g. Sutton et al. 1995) and W3(OH) (e.g. Wyrowski et al. 1999), even though the observed separation is very dependent on source distance.

Gas phase and grain surface chemistry may both play critical roles in the formation of CH_3COOH and other large molecules in the ISM (Hasegawa et al. 1992; Garrod & Herbst 2006; Garrod et al. 2008). However, the exact pathways of CH_3COOH formation in gas phase or on grain surfaces in astronomical environments are still not clear. The apparent spatial coincidence of the emission of complex O and N-containing species with the CH_3COOH emission may suggest a strong correlation with CH_3COOH formation (e.g., Remijan et al. 2004). Another possibility is that CH_3COOH and

large N-bearing species share approximately the same time scale to form in hot cores. Nevertheless, it is important to investigate the spatial relationship between CH_3COOH and the distribution of other complex molecular species. Thus, we also observed methyl formate ($HCOOCH_3$) and ethyl cyanide (CH_3CH_2CN) as proxies to determine the spatial distribution of O and N-bearing species toward our sources in this survey.

To search for regions of CH_3COOH emission and continue to determine its spatial relationship with the distribution of other complex molecular species, we have used the high sensitivity of the Combined Array for Research in Millimeter-wave Astronomy (CARMA) to carry out a CH_3COOH survey toward three more hot cores. The observed sources are G19.61-0.23, G29.96-0.02 and IRAS 16293-2422 and are described in more detail in §2. A complete description of the CARMA observations are described in §3; the results are presented in §4; and in §5 we describe the analysis routine and discuss the implication of these observations with future surveys and chemical formation models.

2. OBSERVED SOURCES

2.1. G19.61-0.23 & G29.96-0.02

G19.61-0.23 (hereafter, G19) is a molecule-rich ultracompact H II region, which includes a high-mass HMC. Numerous molecules have been detected in this region, including OH (Matthews et al. 1977; Garay et al. 1985), H_2O (Genzel & Downes 1977), CH_3OH (Kalenskii et al. 1994; Larionov et al. 1999), NH_3 (Garay et al. 1998), CS (Shirley et al. 2003; Wu & Evans 2003; Larionov et al. 1999), HCN (Wu & Evans 2003) and CO (Hofner et al. 2000). G29.96-0.02 (hereafter, G29) is another high-mass ultracompact region that also has been observed in many molecular species including CH_3CN, $C^{18}O$, CH_3OH, CH_3CH_2CN, $C^{34}S$, CH_3OCH_3, $HCOOCH_3$, ^{34}SO, SO_2, HC_3N, H_2CS, C_2H_5OH and SiO (see e.g. Cesaroni et al. 1998; Olmi et al. 2003; Beuther et al. 2007, and references therein). One of the more recent surveys toward both sources was conducted by Fontani et al. (2007) with the Institute de Radioastronomie Millimétrique 30-m (IRAM) telescope. These observations targeted several emission features between 1 and 3 mm wavelengths of CH_3CH_2CN, vinyl cyanide (CH_2CHCN) and dimethyl ether (CH_3OCH_3). Specifically, the observations by Fontani et al. (2007) were conducted to further investigate whether the so called "chemical differentiation" seen toward Orion and W3 is a general characteristic of high mass HMCs. However, no "chemical differentiation" was observed within the spatial limits defined by the size of the synthesized beam of their observations.

Toward G19, from the observations of a series of CH_3CH_2CN transitions, Fontani et al. (2007) determined a rotational temperature of T_{rot}=116(12) K, and from that a source averaged column density of N_S=2.2(0.3)×10^{16} cm^{-2}. From a series of CH_3OCH_3 transitions that would be used to represent the excitation and distribution of other O-bearing molecules like $HCOOCH_3$, Fontani et al. (2007) determined a T_{rot}=158(17) K, and N_S=2.0(0.2)×10^{15} cm^{-2}. Note that the

half power beam width (HPBW) of the IRAM 30-m telescope ranged in these 1 mm to 3 mm observations from $\sim 12''$ to $\sim 22''$, respectively. In contrast, using archival data from the Submillimeter Array (SMA), Wu et al. (2009) found a much higher temperature for the hot core regions. Using methyl cyanide (CH_3CN) at a spatial resolution of $2''6 \times 2''1$, they found $T_{rot} \sim 552$ K and the beam averaged column density, $N_S \sim 3.4 \times 10^{16}$ cm^{-2} without optical depth corrections.

In a dedicated CH_3COOH survey of high mass HMCs by Remijan et al. (2004), $HCOOCH_3$ (methyl formate), CH_3CH_2CN (ethyl cyanide), CH_3OH (methanol) and $HCOOH$ (formic acid) were all detected at a spatial resolution of $\sim 5''$ toward G19. There was also an indication of weak CH_3COOH emission at 111.507 GHz, at the 1σ detection limit of the BIMA array. Based on the detected CH_3COOH sources and the upper limits from the non-detections, the abundance ratio of CH_3COOH to $HCOOCH_3$ seems universal in high-mass HMCs. If G19 indeed contains CH_3COOH, the $HCOOCH_3$ detection indicated that the CH_3COOH transitions were just slightly lower than the BIMA sensitivity. To clearly detect the CH_3COOH transition lines, we needed a higher sensitivity by a factor of 4, which is provided by CARMA in this survey.

Toward G29, the observations by Fontani et al. (2007) of CH_3CH_2CN transitions yielded a $T_{rot}=121(17)$ K, and from that a $N_S=1.5(0.3)\times 10^{16}$ cm^{-2}. Similarly, observations of CH_3OCH_3 transitions yielded a $T_{rot}=141(26)$ K, and $N_S=6.2(1.0)\times 10^{15}$ cm^{-2}. Another recent campaign toward G29 was by Beuther et al. (2007) who mapped the spatial distribution of several complex molecules with the SMA at a spatial resolution of $\sim 0''4 \times 0''3$. However, no temperature or column density determinations were made from the emission features of these complex molecules. The only reported temperature of the compact emission regions was made from observations of CH_3OH in its vibrationally excited $v_t=1$ state. From the relative intensities of the detected emission features, Beuther et al. (2007) reported an excitation temperature of $T_{ex} \sim 340$ K with a lower limit of 220 K. In addition, this mapping campaign showed the distributions of CH_3OH, CH_3CH_2CN, CH_3OCH_3 and $HCOOCH_3$ were co-spatial suggesting that G29 may be another source of CH_3COOH and that an excitation temperature as high as 220 K may be used in the determination of the column density of these complex molecules (see §3).

2.2.   IRAS 16293-2422

IRAS 16293-2422 is one of the most well-studied and observed low-mass star forming region (e.g., Looney et al. 2000). It consists of two clumps denoted as component A and B (hereafter I16293A and B). The structure of I16293A is much more complex than I16293B (e.g. Chandler et al. 2005). I16293A contains two centimeter sources A1 and A2 (Wootten 1989), and two submillimeter sources Aa and Ab (Chandler et al. 2005). Moreover, I16293A2 may actually be a bipolar ejection with two components (Loinard et al. 2007). Despite their low masses, both component A and B have been suggested to be as molecule-rich as high-mass HMCs (e.g. Schöier et al. 2002; Cazaux et al. 2003).

Large O-bearing species, including $HCOOCH_3$ and $HCOOH$, and N-bearing species, including CH_3CN (methyl cyanide), CH_2CHCN (vinyl cyanide) and CH_3CH_2CN, have been detected toward this region (Cazaux et al. 2003; Bottinelli et al. 2004; Kuan et al. 2004; Remijan & Hollis 2006). With the IRAM 30-m telescope, Cazaux et al. (2003) reported the first detection of CH_3COOH in this low mass region via the $9_{*,9} - 8_{*,8}$ E line at 100.855 GHz. This makes IRAS 16293-2422 the only low-mass CH_3COOH source to date. However, Cazaux et al. (2003) did not detect the counterpart, $9_{*,9} - 8_{*,8}$ A line, and the $9_{*,9} - 8_{*,8}$ E line is known to be blended (e.g., Cazaux et al. 2003). Comparing the IRAM single dish of a $28''$ beam to an estimated source size of $5''$ for the CH_3COOH emission, beam dilution would severely hinder the detection of other weak CH_3COOH lines and may even pick up the extended emission from more distributed molecular species. To further investigate the CH_3COOH distribution toward IRAS 16293-2422, we observed two more CH_3COOH transitions in this survey with the high resolution of CARMA, which is better coupled to the assumed source size and is insensitive to extended emission.

3. OBSERVATIONS

The CH_3COOH survey was carried out with the CARMA $\lambda = 3$ mm receivers from Spring 2006 to Spring 2008 in the B and C configurations. The individual angular resolutions are about $1''$ and $2''$, respectively. Table 1 summarizes the properties of the observed sources, which includes the source positions, flux calibrators, gain calibrators, distances, masses and LSR velocities. The six windows in the CARMA correlator were configured as two wide-band and four narrow-band windows. Each wide-band window has 500 MHz bandwidth and 15 channels while each narrow-band window has 31 MHz bandwidth and 63 channels. The narrow-band high spectral resolution is 0.49 MHz per channel, which provides sufficient sensitivity to resolve the observed transitions and lower the line confusion effect to detect the compact emission from large molecules. The amplitude and phase calibrations were accomplished by observing the gain and flux calibrators. The overall flux calibration uncertainty is 10-15%. The CARMA flux uncertainty discussed in the text is the statistical uncertainty and does not account for any amplitude calibration error. In this paper, we will use the style of showing 1σ statistical uncertainties in parenthesizes after the derived values. During data reduction, pointing and system temperatures were checked to monitor data quality.

We observed the $10_{*,10} - 9_{*,9}$ E and A CH_3COOH lines at 111.507270(20) and 111.548533(20) GHz (Ilyushin et al. 2008) in two narrow band windows. Based on previous observations (Remijan et al. 2002, 2003), they are unblended and have similar line strengths. In addition to CH_3COOH, we included two $HCOOCH_3$ and three CH_3CH_2CN lines in the other narrow-band windows. Table 2 summarizes the observed molecules and their transitions. All spectral line data were taken from the Spectral Line Atlas of Interstellar Molecules (SLAIM) (F. J. Lovas, private communication)[1], the Cologne Database for Molecular Spectroscopy (Müller et al. 2005) and the appropriate laboratory

---

[1]available at http://www.splatalogue.net (Remijan et al. 2007)

references listed therein.

4. RESULTS

The observational data were reduced with the MIRIAD package (Sault et al. 1995). The final data presented in the figures were Hanning-smoothed over 3 channels and continuum-subtracted. The observations in B and C configurations were combined using natural weighting to obtain the best sensitivity and synthesized beams of $\sim 2''$. We present the observations of each source as both maps of the molecular emission and the spectra at the peak of the emission (Figures 1 through 7). The continuum emission maps shown were made from channels contained in the wideband windows which were free from line emission. All of the spectra from each source are shown in rows and columns. In each spectral figure, column (a) displays window 2 (rest frequency=107.54375 GHz); column (b), window 3 (rest frequency=107.59404 GHz); column (c), window 6 (rest frequency=111.50727 GHz); and column (d), window 5 (rest frequency=111.54853 GHz). In row 1, the observed spectra (Hanning smoothed over 3 channels) are overlaid on the modeled spectral line data represented by Gaussians (red trace). In row 2, the modeled spectral line data from row 1 are convolved with the spectral resolution of the original observational data and co-added with 24 mJy/beam random noise. Finally, row 3 presents the residuals from the modeled data subtracted from the observational data (i.e row 1 minus row 2). The maps and spectra are discussed below.

4.1. G19.61-0.23

One of the most relevant discoveries in this paper is the new detection of CH_3COOH toward G19 that highlights the importance of interferometric observations in the detection of weak spectral signatures confined in compact emission regions. To illustrate the distribution of the CH_3COOH emission toward G19, we have summed the intensity of the CH_3COOH lines to produce a combined CH_3COOH contour map which is overlaid on the continuum map in grayscale in Figure 1(a). Both the $10_{*,10} - 9_{*,9}$ E and $10_{*,10} - 9_{*,9}$ A lines were detected in the two CH_3COOH spectral windows (Figures 2(c) and (d)) at the canonical v_{LSR} of 40 km s^{-1} for G19. While some weak unidentified lines may appear in the windows after Hanning smoothing, the relative line strengths of the two CH_3COOH transitions are roughly equal as predicted by rotational spectroscopy. G19 consists of several high density components of continuum emission between 2 cm and 3 mm wavelengths (Furuya et al. 2005). In this case, the CH_3COOH emission is located near the center of component C and the CH_3COOH emission region has an effective scale size of $2''$.

In addition to CH_3COOH, we have observed transitions of $HCOOCH_3$ and CH_3CH_2CN. Two transitions of $HCOOCH_3$, $9_{2,8} - 8_{2,7}$ A/E and three transitions of CH_3CH_2CN, $12_{4,9} - 11_{4,8}$, $12_{4,8} - 11_{4,7}$, and $12_{3,10} - 11_{3,9}$ are shown in Figures 2(a) and (b). All transitions are at a $v_{LSR}=40$ km s^{-1}. The statistical significance of three possible unidentified lines will be discussed in Section

5.5. The HCOOCH$_3$ map (Figure 1(b)) and CH$_3$CH$_2$CN map (Figure 1(c)) show emission that peaks primarily near component C, like the CH$_3$COOH emission, yet with a southward projection toward component A that was not seen in the lower resolution BIMA observations (Remijan et al. 2004). Table 3 summarizes the fitting results of the detected transitions towards G19. In our fitting routine, we assume that the rest frequencies of each molecular transition is fixed to the v_{LSR} of the source and the HCOOCH$_3$ transition that is blended with the CH$_3$CH$_2$CN transition shares the same linewidth and peak intensity as the unblended transition. Also, shown are the line widths and intensities of the model data for a direct comparison.

4.2. G29.96-0.02

We have detected HCOOCH$_3$ and CH$_3$CH$_2$CN toward G29. Figures 3(a) and (b) show the distribution of HCOOCH$_3$ and CH$_3$CH$_2$CN emission toward the G29 region, respectively. In Figure 4, we clearly detected the two blended pairs of transitions of HCOOCH$_3$ $9_{2,8} - 8_{2,7}$ E/A and CH$_3$CH$_2$CN $12_{4,9} - 11_{4,8}$ and $12_{4,8} - 11_{4,7}$. The spectrum is very similar to that of G19 (Figure 2(a)). The CH$_3$CH$_2$CN $12_{3,10} - 11_{3,9}$ transition and possible U lines in Figure 4(b), also have similar profiles to those in Figure 2(b).

G29 consists of two main continuum peaks at 1.2 cm, which trace the UCH II region, and at 862 μm, which trace the cloud core (Beuther et al. 2007). The cloud core is the location of the molecular emission; however, the emission is not bright enough to contribute significantly at 3 mm wavelengths. In Figure 3 the continuum emission is dominated by the UC H II region.

Figure 4(c) and (d) shows the two CH$_3$COOH spectral windows toward G29. Unlike the data from G19, there are no statistically significant features at the CH$_3$COOH rest frequencies. There is a 1σ feature that may be due to the $10_{*,10} - 9_{*,9}$ E transition of CH$_3$COOH, but the corresponding $10_{*,10} - 9_{*,9}$ A transition is noticeably absent. In the discussion, we will investigate these passbands more closely with respect to the modeled data. Table 4 summarizes the fitting results of the detected transitions towards G29. The fitting criteria and model predictions are presented in the same manner as in Table 3.

4.3. IRAS 16293-2422

Unlike the spectra from Cazaux et al. (2003), we resolved IRAS 16293-2422 into I16293A and B with our $3''.1\times$ $1''.9$ beam (see Figure 5). Therefore, beam dilution in this observation is minimized. Figure 6 and 7 shows the two CH$_3$COOH spectral windows toward I16293A and I16293B, respectively. Toward I16293A, we detect weak emission features that may be due to transitions of CH$_3$COOH but they are right at the 2σ detection limit. Toward I16293B, as in G29, there are no statistically significant features at the CH$_3$COOH rest frequencies. There are 1σ features that may be due to the $10_{*,10} - 9_{*,9}$ A/E transitions in these Hanning smoothed data, but

nothing convincing beyond that level. In §5.5 we evaluate whether the features toward I16293A may be due to CH_3COOH.

We have also observed two new transitions of $HCOOCH_3$. The line profiles of $HCOOCH_3$ shown in Figure 6 toward I16293A are wider and may be suffering from self absorption (Remijan & Hollis 2006) more than the line profiles shown in Figure 7 toward I16293B, which are much more narrow. This suggests that I16293A and I16293B may have distinguishable molecular dynamics. Figure 5 (a) and (b) show the distribution of $HCOOCH_3$ emission with respect to the 3 mm continuum emission toward the I16293A & B regions, respectively. Table 5 summarizes the fitting results of the detected transitions towards IRAS 16293-2422. The fitting criteria and model predictions are presented in the same manner as in Table 3.

5. ANALYSIS & DISCUSSION

5.1. Molecular Column Densities

Molecular column density is one essential physical parameter needed to constrain chemical models (see e.g. Garrod et al. 2008 and references therein). In order to determine the column densities of each molecular species of interest, we assume that each region has uniform physical conditions, that the populations of the energy levels can be characterized by a Boltzmann distribution, and finally, that the emission is optically thin. Assuming that the molecular species is in local thermodynamic equilibrium (LTE) and low optical depth, the total beam averaged column density is

$$N_T(\mathrm{cm}^{-2}) = 2.04 \times 10^{20} \frac{\int I(\mathrm{Jy\ beam}^{-1}) d\upsilon (\mathrm{km\ s}^{-1}) Q_r e^{E_u(K)/T_r}}{\Omega_b(\mathrm{arcsec}^2) \nu^3 (\mathrm{GHz}^3) <S\mu^2> (\mathrm{debye}^2)}, \tag{1}$$

where Ω_b is the solid angle of the beam , $\int I_\upsilon d\upsilon$ is the integral of the line intensity over velocity, ν is the spectral line frequency, $<S\mu^2>$ is the line strength parameter, Q_r is the rotational partition function, T_r is the rotational temperature, and E_u is the upper level energy of the transition (Miao et al. 1995). In each case, we assume the source emission fills the synthesized beam of the observations. All of the line parameters used for the analysis are given in Table 2.

A least-square fitting routine with Gaussian functions was used to determine the linewidths (Δv), peak intensities (ΔI) and $\int I d\upsilon$ of each observed spectral line toward each source. All least-square fitting was done using the standard packages contained in the *Mathematica* software package. Using the spectroscopic parameters from Table 2 and by varying the temperature and column density over a wide range of values (e.g. the temperature range investigated was from 10-500 K and the column density range was from 10^{12} - 10^{18} cm^{-2} for each molecular species), Equation (1) gave a predicted integrated line intensity for each spectral line observed in our data. These predictions of integrated line intensity were then compared to the measured values and, using a least-squares fitting routine, a best fit temperature and column density was found for each molecule toward each source. However, there were some sources where an independent fit of the

temperature did not converge. These sources are described in more detail in the following sections. Columns 3 and 4 of Table 3, 4 and 5 give the fitted line parameters of the observed peak intensity and line width. Columns 5 and 6 give the modeled peak intensity based on the least square fitting routine and the fitted line width from the observed data, respectively. Once all the relevant line parameters have been determined, a model spectrum with the appropriate amount of random noise added and convolved with the spectral resolution of the observation can then be produced and be directly compared with the observed dataset (see §5.5).

The rotational temperature T_r generally is representative of the physical kinetic temperature in regions where the spatial density is larger than the critical density of the molecule in question. The assumption in this work is that the densities of the HMCs investigated are expected to be high enough for this to be true for these molecules. The rotational temperature is often found by observing several different transitions of a molecular species over a range of E_u values. However, given the limited bandwidth and low number of transitions observed in our data, it was often difficult to accurately constrain the temperature and column density of our three observed molecules toward these regions (e.g., Snyder et al. 2005). Therefore, when the least squares fit failed to give a reasonable temperature for a given molecular species, we adopted a rotational temperature from previous observations by other investigators toward these sources at similar spatial resolution and were then able to fit for the total beam averaged column densities or associated upper limits if no transitions were detected beyond the statistically significant 1σ limit. It was also the case that if the fitting procedure was given too many free parameters, a constraint was needed on one or more or else it would not converge (see the G29 discussion below). To properly constrain the temperature of these regions over a variety of molecular species, observations of additional transitions are necessary and complete spectral line surveys may be required (see e.g. Fontani et al. 2007; Friedel et al. 2004, and references therein).

For the G19 region, the least square fitting routine determined a rotational temperature of CH_3CH_2CN of $T_{rot}=161(58)$ K, and a beam averaged column density of $N_T=6(3)\times10^{16}$ cm^{-2}. The errors on all fits are 1σ. The routine could not find a reasonable fit for the temperature and column density for either $HCOOCH_3$ or CH_3COOH presumably because the detected transitions were too close in energy. Therefore, because the emission regions of each molecular species around G19 are nearly co-spatial (Figure 1), we adopted the same rotational temperature for $HCOOCH_3$ and CH_3COOH as found from the CH_3CH_2CN fit. Assuming a $T_{rot}=161$ K for $HCOOCH_3$, we find a best fit to the column density of $N_T=9(2)\times10^{16}$ cm^{-2} and for CH_3COOH, we find a best fit to the column density of $N_T=2(1)\times10^{16}$ cm^{-2}. Given the minimum and maximum values of the measured column density, we determine an abundance ratio range of $N_{HCOOCH_3}/N_{CH_3COOH}=3\text{-}11$. Table 3 gives the fitted intensities of each of the detected spectral features compared to the predicted intensities determined from Equation (1) for G19.

For the G29 region, the least square fitting routine determined a rotational temperature of CH_3CH_2CN of $T_{rot}=107(49)$ K, and a beam averaged column density of $N_T=1.1(7)\times10^{16}$ cm^{-2} only if we adopted a rotational temperature of 150 K, determined from Olmi et al. (2003) and

supported by the observations of Fontani et al. (2007) and Beuther et al. (2007), for the transitions of HCOOCH$_3$. This temperature was also set to determine the upper limit for the column density of CH$_3$COOH. Assuming a T$_{rot}$=150 K for HCOOCH$_3$, we find a best fit to the column density of N$_T$=4(1)×10^{16} cm^{-2} and for CH$_3$COOH, we find an upper limit to the column density of N$_T$<9×10^{14} cm^{-2} for a relative abundance ratio upper limit of N$_{HCOOCH_3}$/N$_{CH_3COOH}$>50. Table 4 gives the fitted intensities of each of the detected spectral features compared to the predicted intensities determined from equation (1) for G29. We also note the detection of another feature shown in Figure 2 near 107.540 GHz that is most likely due to two high energy (>110 K) spectral lines of CH$_3$CH$_2$CN. The discussion of weak spectral features near the 1σ noise level will be given in section §5.5.

A recent observation of the G19 and G29 regions with the IRAM 30-m telescope (Fontani et al. 2007) covered our two acetic acid line frequencies (Figure 8). However, with a 28″ beam, the lines detected are under the noise level of 26 mK. These lines are brighter than those observed by Cazaux et al. (2003), but the beam dilution is severe. The high resolution capability of CARMA is indeed critical for searching for acetic acid and large molecule research.

Finally, toward IRAS 16293-2422, the least square fitting routine could not determine a rotational temperature for the detected transitions of HCOOCH$_3$ presumably for the same reason as described toward G19. Thus, we adopted a rotational temperature of 62 K determined from Bottinelli et al. (2004). In this case, we find a best fit to the column density of HCOOCH$_3$ of N$_T$=1.5(3)×10^{16} cm^{-2} toward region A and 6(1)×10^{15} cm^{-2} toward region B. Since there was no clear detection of CH$_3$CH$_2$CN beyond the 1σ detection limit toward either region A or B, based on the noise level in each of the passbands containing those lines, we determined an upper limit to the total beam averaged column density of CH$_3$CH$_2$CN to be <6×10^{13} cm^{-2} for region A; and <3×10^{14} cm^{-2} toward region B. For CH$_3$COOH, the 2σ detection toward region A gives a total beam averaged column density of ∼1.6×10^{15} cm^{-2} and for region B, we determine and upper limit of <6×10^{14} cm^{-2}. Table 5 summarizes the fitting results of the HCOOCH$_3$ transitions compared to the model intensities determined from Equation (1).

5.2.   A Proxy for the Detection of CH$_3$COOH Sources

We have successfully detected CH$_3$COOH toward G19. Following Sgr B2(N-LMH), W51e2 and G34.3+0.15, G19.61-0.23 is the fourth high mass hot core that is a source of CH$_3$COOH. We compare the CH$_3$COOH column densities and the abundance ratios to HCOOCH$_3$ of all detected CH$_3$COOH hot cores in Table 7. The values are generally consistent. Therefore, the column densities and ratios can be used to constrain hot core chemical models assuming the co-spatial dependence of HCOOCH$_3$ and CH$_3$COOH remains. This has yet to be tested at extremely high spatial resolution. In addition, a consistency can be found between all the sources containing CH$_3$COOH emission by comparing the relative line strengths between the detected transitions of HCOOCH$_3$ and CH$_3$CH$_2$CN to the CH$_3$COOH emission. Taking a ratio between measured (or predicted inten-

sities) of the 107.594 GHz line of CH_3CH_2CN to the 111.507 GHz line of CH_3COOH, we find that this ratio is between 5.5 and 6 for those sources where CH_3COOH is detected. Therefore, given the line intensity of 0.21 Jy/beam for the 107.594 GHz line of CH_3CH_2CN toward G29.96-0.02, the expected line intensity for the 111.507 GHz line of CH_3COOH is ≤0.04 Jy/beam. This intensity is right at the 1σ detection limit of the current CARMA observations. Therefore, in addition to the criteria for the detection of CH_3COOH outlined in Remijan et al. (2003), we now have a good proxy for the detectability of the 111 GHz CH_3COOH transitions relative to the detected line strengths of the $HCOOCH_3$ and CH_3CH_2CN transitions near 107 GHz. Further observations of new sources of $HCOOCH_3$ and CH_3CH_2CN that fit the criteria set by Remijan et al. (2003) and higher S/N observations of sources like G29, are necessary to validate this hypothesis.

5.3. CH_3COOH in IRAS 16293-2422?

High spatial resolution maps and spectra of IRAS 16293-2422 clearly reveal that the morphologies of the emission of complex molecules are clearly not co-spatial and that there is no simple separation of O and N-bearing "chemical differentiation" (Guélin et al. 2008). Blake et al. (1987) and Rodgers & Charnley (2001) have suggested the difference in the morphologies of the emission of complex molecules in these regions reflects the timescales of chemical evolution. Predominantly N-bearing species (e.g. CH_3CH_2CN) represent the later stage of chemical evolution while predominantly O-bearing species (e.g. $HCOOCH_3$) represent the earlier stage. Their models can estimate the ages of hot cores by comparing this difference between the O and N morphology of emission. However, to date, no direct observation can accurately measure hot core ages, so the uncertainty of these estimates is large.

IRAS 16293-2422 also shows clear distinctions in the morphology of molecular emission (Chandler et al. 2005; Remijan & Hollis 2006). In fact, the relative distributions of molecular species will undoubtedly give insight into their formation chemistry. It may also turn out that the relative abundances of molecular species and the overall population of energy levels of the detected transitions of a given molecule may be determined more by the formation chemistry and not on the local thermodynamic environment. To test this hypothesis will require high spectral and spatial resolution observations of a group of species that may form via a common formation pathway.

IRAS 16293-2422 has been reported as the first low-mass CH_3COOH source by Cazaux et al. (2003) using the IRAM 30-m telescope, but the one detected line was likely blended. While IRAS 16293-2422 is not resolved in their work (beamsize of $28''$), we have resolved it into I16293A and B with a separation of less than $5''$. Even though their observation used different transitions, we should detect our CH_3COOH lines in our synthesized beam of $3.''1 \times 1.''9$ using their flux estimates. Although at a lower flux than expected from their results, we do detect two CH_3COOH transitions toward region A but only at the 2σ limit. We estimate a column density of $\sim 1.6 \times 10^{15}$ cm^{-2}, and Cazaux et al. (2003) estimated an upper limit of 2.5×10^{15} cm^{-2}, which is similar.

Furthermore, there is no evidence beyond the 1σ levels of any emission of CH_3COOH toward region B. In addition, while we have observed $HCOOCH_3$ in I16293A and B, we did not detect the corresponding CH_3CH_2CN emission features. The detection of CH_3COOH toward G19 (and possibly toward I16293A) and the other hot cores have demonstrated that a diversity of abundant large O and N-bearing species are strongly correlated with CH_3COOH. One possibility is that the mix of O and N-bearing species may serve as an efficient chemical network for CH_3COOH and other large molecules. Thus, they need to wait for large N-bearing molecules to form first before they can be efficiently produced. Another possibility is that the formation of large O and N-bearing species is simply time dependent, and the gas-phase CH_3COOH concentration just by coincidence starts to increase along with large N-bearing species. Given the criteria set above, it is intriguing that CH_3COOH is detected toward I16293A given there was no clear evidence of any emission from CH_3CH_2CN. Further higher sensitivity observations are once again necessary to confirm this detection and determine the evolutionary stage of the I16293A and B cores.

5.4. CH_3COOH Formation

Both gas phase and grain surface chemistry undoubtedly play important roles in hot cores (e.g. Hasegawa et al. 1992; Garrod & Herbst 2006; Garrod et al. 2008). Large molecule abundances can be enhanced enormously by grain surface chemistry while current models of gas phase chemistry alone are not sufficient to match observations. Garrod & Herbst (2006) have demonstrated that radicals in the icy mantles on grain surfaces can move around as the temperature gradually increases from 10 to 200 K in star forming regions. Grain surfaces become efficient environments for large molecules to form. However, the details of CH_3COOH formation in hot cores still remain unclear. The correlation between CH_3COOH and large N-bearing molecules may suggest that some N-bearing molecules act as catalysts to the CH_3COOH formation. The chemical and physical evolution timescales of star formation lacks direct observational evidence to confirm chemical models. Without the support of observation, it is difficult to establish solid chemical models. Garrod et al. (2008) have reported their new chemical model for CH_3COOH in hot cores. Grain surface reactions have been enhanced to match observations. They show the time scales of hot cores warming up affect the abundances of the secondary radical CH_3CO, which can react with OH to form CH_3COOH. This effect can also cause the dissimilar abundances of structural isomers, which is consistent with our survey.

5.5. Identifying Weak Spectral Features Using Model Spectra.

When CH_3COOH was first detected (Mehringer et al. 1997), it emphasized the importance of interferometry for the study of astrochemistry in hot cores. Star forming regions generally contain many regions of compact molecular emission. Although G19 has a complex structure, including extended and compact components (see Furuya et al. 2005), the CH_3COOH detection

toward G19 was conducted with a high resolution beam, $1\rlap{.}''9 \times 1\rlap{.}''6$, which is the smallest used in a CH_3COOH survey to date. The three observed molecules in G19, CH_3COOH, $HCOOCH_3$ and CH_3CH_2CN, are mainly located at the same component, which agrees with the CH_3CH_2CN observation by Furuya et al. (2005). As we continue extending CH_3COOH surveys to smaller hot cores, the required resolution of observations will be higher.

Higher resolution observations also have the advantage of reducing the effect of line confusion present in a spectrum. Also, if the source size of the emitting region is well coupled to the synthesized beam of the array, weak spectral features that are lost due to beam dilution effects from single dish observations can be significantly resolved out of the noise. Thus, many new molecule detections over the last several years have used both a combination of single dish and array observations to confirm the detection (e.g., Belloche et al. 2008, 2009). In addition, these detections routinely use model spectra based on the laboratory and calculated rotational spectroscopy of energy levels and line strengths for molecular transitions, the physical conditions of the emitting regions including temperature and density and finally, the characteristics of the telescope including forward beam efficiency and field of view (i.e. beam size). Given the model spectra, the weak transitions of molecular species appear statistically significant in the observed spectrum. However, the model data have near infinite spectral resolution compared to the observed data and do not include an estimate of the noise level in the passband. These types of models are shown in the spectral line data presented in this work (red Gaussian traces in the first row of spectra in Figures 2, 4, 6 and 7).

In order to correctly ascertain whether a weak feature in the observed spectrum is due to a calculated line of a molecular species, we advocate taking the model data and convolving it with the spectral resolution of the instrument and adding the appropriate amount of random noise to the resultant spectrum to give a more accurate representation of the data collected by the telescope. The noise level is based on the measured noise of line free channels in the observed data. These modeled data are then subtracted from the observed data to form a residual spectrum. From these residuals, with the caveat of an accurate model of the physical conditions of the source, one can identify the remaining weak spectral features and determine if features close to the 1-2σ level are in fact statistically significant spectral line features.

Based on the residual passbands shown in the last row of Figures 2, 4, 6 and 7, we include in Tables 3, 4 and 5 the possibility of unidentified lines (i.e. U-lines) in the data toward G19, G29 and IRAS 16293-2422. In addition, given the spectral line fit (red Gaussian traces) toward IRAS 16293-2422, there is a suggestion that the weak emission features shown toward I16293B may in fact be due to CH_3COOH. However, when this model spectrum is convolved with the noise level in the passband, these weak features completely disappear and there are definitely no statistically significant feature seen in the residual passbands. As a result, while we claim that the emission features that are coincident with the CH_3COOH transitions toward I16293A are in fact from CH_3COOH, these features are only barely above the noise level so further high sensitivity observations are needed for a definitive detection.

It is our recommendation that if model spectra are going to be the new proxy for identifying weak spectral features in observational data, the model data should be first convolved to the spectral resolution of the telescope and the appropriate amount of noise be added to the model in order to make an accurate representation as possible to the observed data. Only then can the 1-2σ spectral features be corrected assessed as statistically significant features in the observed data and not an artifact of the noise and spectral resolution.

6. SUMMARY

We have conducted a high resolution acetic acid (CH_3COOH) survey at 3 mm wavelengths for the first time with CARMA towards two high-mass hot cores, G19.61-0.23 and G29.96-0.02, and a low-mass embedded protostar system, IRAS 16293-2422. We have detected CH_3COOH emission in G19.61-0.23, via the two CH_3COOH rotational transitions, $10_{*,10} - 9_{*,9}$ E and A. While G19.61-0.23 consists of several clumps, high resolution mapping reveals that the CH_3COOH emission is extremely compact ($<2''$) toward component C. Methyl formate ($HCOOCH_3$) and ethyl cyanide (CH_3CH_2CN) were also detected. The emission from these two molecules is more extended than the CH_3COOH emission but the peaks of all three emission spectra are toward component C. The CH_3COOH column density and abundance ratio with respect to methyl formate ($HCOOCH_3$), are $2.0(1.0)\times10^{16}$ cm^{-2} and $2.2(0.1)\times10^{-1}$ respectively, which is higher but comparable to the other high-mass CH_3COOH sources given the current level of detection. Although acetic acid is not detected toward G29.96-0.02, we have detected $HCOOCH_3$ and CH_3CH_2CN. The $HCOOCH_3$ and CH_3CH_2CN emission features of G29.96-0.02 are weaker than G19.61-0.23 by a factor of 3. While we detect CH_3COOH in G19.61-0.23, the non-detection of CH_3COOH in G29.96-0.02 may be due to the limited sensitivity. Finally we have detected two new transitions of $HCOOCH_3$, $9_{2,8} - 8_{2,7}$ E and A toward IRAS 16293-2422 and weak emission features at the 2σ level of CH_3COOH toward I16293A. This is the first observation of new spectral features of CH_3COOH since the reported detection by Cazaux et al. (2003). The $HCOOCH_3$ spectrum toward I16293B shows narrower and more distinguishable line profiles than the spectrum toward I16293A, which may be suffering from self-absorption. However, we did not detect CH_3CH_2CN in IRAS 16293-2422 at the the 1σ detection limit.

The new CH_3COOH detection demonstrates the strong correlation between large O and N-bearing species and CH_3COOH in hot cores. The timescale of hot cores may also play a role in O/N chemical differentiation and hence CH_3COOH formation. However, we need more CH_3COOH detections to confirm these suggestions. The compactness of the emission from large molecules stresses the need of interferometers for hot core chemistry observations. Our high resolution survey has provided critical information about the chemical and physical properties of hot cores, which can be used to constrain the hot core chemical models. Higher resolution observations are still required to precisely determine temperature and the density distribution of large O and N-bearing species for physical-parameter sensitive chemical models. Through well-improved chemical models,

we can better understand the distinctive hot core chemistry.

REFERENCES

Belloche, A., Garrod, R. T., Müller, H. S. P., Menten, K. M., Comito, C., & Schilke, P. 2009, A&A, 499, 215

Belloche, A., Menten, K. M., Comito, C., Müller, H. S. P., Schilke, P., Ott, J., Thorwirth, S., & Hieret, C. 2008, A&A, 492, 769

Beuther, H., Zhang, Q., Bergin, E. A., Sridharan, T. K., Hunter, T. R., & Leurini, S. 2007, A&A, 468, 1045

Blake, G. A., Sutton, E. C., Masson, C. R., & Phillips, T. G. 1987, ApJ, 315, 621

Bottinelli, S., et al. 2004, ApJ, 617, L69

Cazaux, S., Tielens, A. G. G. M., Ceccarelli, C., Castets, A., Wakelam, V., Caux, E., Parise, B., & Teyssier, D. 2003, ApJ, 593, L51

Cesaroni, R., Hofner, P., Walmsley, C. M., & Churchwell, E. 1998, A&A, 331, 709

Chandler, C. J., Brogan, C. L., Shirley, Y. L., & Loinard, L. 2005, ApJ, 632, 371

Di Francesco, J., Myers, P. C., Wilner, D. J., Ohashi, N., & Mardones, D. 2001, ApJ, 562, 770

Fontani, F., Pascucci, I., Caselli, P., Wyrowski, F., Cesaroni, R., & Walmsley, C. M. 2007, A&A, 470, 639

Friedel, D. N., Snyder, L. E., Turner, B. E., & Remijan, A. 2004, ApJ, 600, 234

Fukuyama, Y., Odashima, H., Takagi, K., & Tsunekawa, S. 1996, ApJS, 104, 329

Furuya, R. S., Cesaroni, R., Takahashi, S., Momose, M., Testi, L., Shinnaga, H., & Codella, C. 2005, ApJ, 624, 827

Garay, G., Moran, J. M., Rodriguez, L. F., & Reid, M. J. 1998, ApJ, 492, 635

Garay, G., Reid, M. J., & Moran, J. M. 1985, ApJ, 289, 681

Garrod, R. T., & Herbst, E. 2006, A&A, 457, 927

Garrod, R. T., Weaver, S. L. W., & Herbst, E. 2008, ApJ, 682, 283

Gaume, R. A., Claussen, M. J., de Pree, C. G., Goss, W. M., & Mehringer, D. M. 1995, ApJ, 449, 663

Genzel, R., & Downes, D. 1977, A&AS, 30, 145

Goldsmith, P. F., & Langer, W. D. 1999, ApJ, 517, 209

Guélin, M., Brouillet, N., Cernicharo, J., Combes, F., & Wooten, A. 2008, Ap&SS, 313, 45

Hasegawa, T. I., Herbst, E., & Leung, C. M. 1992, ApJS, 82, 167

Hofner, P., Wyrowski, F., Walmsley, C. M., & Churchwell, E. 2000, ApJ, 536, 393

Ilyushin, V., Kleiner, I., & Lovas, F. J. 2008, Phys. Chem. Ref. Data, 37, 97

Kalenskii, S. V., Berulis, I. I., Val'tts, I. E., Dzura, A. M., Slysh, V. I., & Vasil'kov, V. I. 1994, AZh, 71, 51

Kuan, Y.-J., et al. 2004, ApJ, 616, L27

Larionov, G. M., Val'tts, I. E., Winnberg, A., Johansson, L. E. B., Booth, R. S., & Golubev, V. V. 1999, A&AS, 139, 257

Loinard, L., Chandler, C. J., Rodríguez, L. F., D'Alessio, P., Brogan, C. L., Wilner, D. J., & Ho, P. T. P. 2007, ApJ, 670, 1353

Looney, L. W., Mundy, L. G., & Welch, W. J. 2000, ApJ, 529, 477

Matthews, H. E., Goss, W. M., Winnberg, A., & Habing, H. J. 1977, A&A, 61, 261

Mehringer, D. M., Snyder, L. E., Miao, Y., & Lovas, F. J. 1997, ApJ, 480, L71

Miao, Y., Mehringer, D. M., Kuan, Y.-J., & Snyder, L. E. 1995, ApJ, 445, L59

Müller, H. S. P., Schlöder, F., Stutzki, J., & Winnewisser, G. 2005, Journal of Molecular Structure, 742, 215

Oesterling, L. C., Albert, S., De Lucia, F. C., Sastry, K. V. L. N., & Herbst, E. 1999, ApJ, 521, 255

Olmi, L., Cesaroni, R., Hofner, P., Kurtz, S., Churchwell, E., & Walmsley, C. M. 2003, A&A, 407, 225

Remijan, A., Shiao, Y.-S., Friedel, D. N., Meier, D. S., & Snyder, L. E. 2004, ApJ, 617, 384

Remijan, A., Snyder, L. E., Friedel, D. N., Liu, S.-Y., & Shah, R. Y. 2003, ApJ, 590, 314

Remijan, A., Snyder, L. E., Liu, S.-Y., Mehringer, D., & Kuan, Y.-J. 2002, ApJ, 576, 264

Remijan, A. J., & Hollis, J. M. 2006, ApJ, 640, 842

Remijan, A. J., Markwick-Kemper, A., & ALMA Working Group on Spectral Line Frequencies. 2007, in Bulletin of the American Astronomical Society, Vol. 38, Bulletin of the American Astronomical Society, 963

Rodgers, S. D., & Charnley, S. B. 2001, ApJ, 546, 324

Sault, R. J., Teuben, P. J., & Wright, M. C. H. 1995, in Astronomical Society of the Pacific Conference Series, Vol. 77, Astronomical Data Analysis Software and Systems IV, ed. R. A. Shaw, H. E. Payne, & J. J. E. Hayes, 433

Schöier, F. L., Jørgensen, J. K., van Dishoeck, E. F., & Blake, G. A. 2002, A&A, 390, 1001

Shirley, Y. L., Evans, II, N. J., Young, K. E., Knez, C., & Jaffe, D. T. 2003, ApJS, 149, 375

Snyder, L. E. 2006, Proceedings of the National Academy of Science, 103, 12243

Snyder, L. E., Kuan, Y., & Miao, Y. 1994, in Lecture Notes in Physics, Berlin Springer Verlag, Vol. 439, The Structure and Content of Molecular Clouds, ed. T. L. Wilson & K. J. Johnston, 187

Snyder, L. E., et al. 2005, ApJ, 619, 914

Sutton, E. C., Peng, R., Danchi, W. C., Jaminet, P. A., Sandell, G., & Russell, A. P. G. 1995, ApJS, 97, 455

Wootten, A. 1989, ApJ, 337, 858

Wu, J., & Evans, II, N. J. 2003, ApJ, 592, L79

Wu, Y., Qin, S., Guan, X., Xue, R., Ren, Z., Liu, T., Huang, M., & Chen, S. 2009, ApJ, 697, L116

Wyrowski, F., Schilke, P., Walmsley, C. M., & Menten, K. M. 1999, ApJ, 514, L43

Table 1.   Observed Sources

Source	α (J2000.0)	δ (J2000.0)	Flux Calibrator	Gain Calibrator	Distance (kpc)	Mass ($M_\odot$)	v_{LSR} (km s^{-1})
G19.61-0.23[a]	18 27 38.1	-11 56 39.0	Neptune	1911-201	3.50	450	40.0
G29.96-0.02[b]	18 46 04.0	-02 39 21.5	Neptune	1751+096	6.0	1100	98.8
IRAS 16293-2422[c,d]	16 32 22.8	-24 28 33.0	MWC349	1625-254	0.16	5.4	3.9
				1733-130			

[a]Furuya et al. (2005)

[b]Olmi et al. (2003)

[c]Schöier et al. (2002)

[d]Di Francesco et al. (2001)

Table 2.   OBSERVED MOLECULES AND TRANSITIONS

Species	Rotational Partition Function	Transition	Frequency (MHz)	E_u (K)	$< S_{j,j}\mu^2 >$ (debye^2)
CH_3COOH[a]	$Q_r = 14.1T_r^{3/2}$	$10_{*,10} - 9_{*,9}$ E	111,507.270(20)	30.5	54.8
		$10_{*,10} - 9_{*,9}$ A	111,548.533(20)	30.5	54.8
$HCOOCH_3$[b]	$Q_r = 12.45T_r^{3/2}$	$9_{2,8} - 8_{2,7}$ E	107,537.189(25)	28.8	22.8
		$9_{2,8} - 8_{2,7}$ A	107,543.746(25)	28.8	22.8
CH_3CH_2CN[c]	$Q_r = 7.17T_r^{3/2}$	$12_{11,2} - 11_{11,1}$	107,539.854 (3)	167.8	28.4
		$12_{11,1} - 11_{11,0}$	107,539.854 (3)	167.8	28.4
		$12_{4,9} - 11_{4,8}$	107,543.918 (3)	51.4	158.1
		$12_{4,8} - 11_{4,7}$	107,547.593 (3)	51.4	158.1
		$12_{3,10} - 11_{3,9}$	107,594.040 (3)	43.6	166.8

Note. — The 1σ uncertainty of the frequencies is in units of kHz. Each of the CH_3COOH lines consists of two a-type and two b-type transitions. This is represented by an asterisk substituted for the K_- quantum numbers.

[a]Ilyushin et al. (2008)

[b]Oesterling et al. (1999)

[c]Fukuyama et al. (1996); Remijan et al. (2007)

Table 3.   DETECTED MOLECULES AND TRANSITIONS TOWARD G19.61-0.23

Species	Transition	ΔI (Jy beam^{-1})	Δv (km s^{-1})	ΔI (Jy beam^{-1})	Δv (km s^{-1})
		Fitted Data		Model Data	
CH_3COOH	$10_{*,10} - 9_{*,9}\ E$	0.07±0.01	6.4±0.9	0.10	6.4
	$10_{*,10} - 9_{*,9}\ A$	0.09±0.02	6.4±0.9	0.12	6.4
$HCOOCH_3$	$9_{2,8} - 8_{2,7}\ E$	0.20±0.02	6.4±0.9	0.18	6.4
	$9_{2,8} - 8_{2,7}\ A$	0.20±0.02	6.4±0.9	0.18	6.4
CH_3CH_2CN	$12_{11,*} - 11_{11,*}$	0.18±0.02	12.9±0.4	0.13	12.9
	$12_{4,9} - 11_{4,8}$	0.59±0.02	12.9±0.4	0.66	12.9
	$12_{4,8} - 11_{4,7}$	0.59±0.02	12.9±0.4	0.66	12.9
	$12_{3,10} - 11_{3,9}$	0.71±0.01	12.9±0.4	0.72	12.9
U107.588	107.5880 GHz	0.16±0.04	5.6±1.6		
U107.591	107.5910 GHz	0.27±0.03	7.8±1.2		
U107.597	107.5970 GHz	0.31±0.03	12.5±1.2		
U107.604	107.6040 GHz	0.23±0.03	11.1±1.5		
U111.506	111.5055 GHz	0.06±0.02	5.2±1.7		
U111.510	111.5095 GHz	0.07±0.01	17.2±4.5		
U111.546	111.5460 GHz	0.07±0.01	8.7±2.0		

Note. — The $HCOOCH_3$ lines were fit assuming the same linewidth. The same line width fitting criteria applies for the CH_3CH_2CN and CH_3COOH lines. For simplicity, the two CH_3CH_2CN lines listed in Table 2 are now represented as one by an asterisk substituted for the K_- quantum numbers. The other three CH_3CH_2CN lines remain unchanged.

Table 4.   DETECTED MOLECULES AND TRANSITIONS TOWARD G29.96-0.02

Species	Transition	ΔI (Jy beam^{-1})	Δv (km s^{-1})	ΔI (Jy beam^{-1})	Δv (km s^{-1})
		Fitted Data		Model Data	
CH_3COOH	$10_{*,10} - 9_{*,9}\ E$	∼0.04			
	$10_{*,10} - 9_{*,9}\ A$	<0.03			
$HCOOCH_3$	$9_{2,8} - 8_{2,7}\ E$	0.08±0.01	7.8±1.1	0.09	7.8
	$9_{2,8} - 8_{2,7}\ A$	0.08±0.01	7.8±1.1	0.09	7.8
CH_3CH_2CN	$12_{11,*} - 11_{11,*}$	0.07±0.01	10.8±0.4	0.03	10.8
	$12_{4,9} - 11_{4,8}$	0.21±0.01	10.8±0.4	0.23	10.8
	$12_{4,8} - 11_{4,7}$	0.21±0.01	10.8±0.4	0.23	10.8
	$12_{3,10} - 11_{3,9}$	0.27±0.01	10.8±0.4	0.26	10.8
U107.591	107.5910 GHz	0.11±0.01	8.5±0.9		
U107.597	107.5975 GHz	0.08±0.01	10.8±1.2		
U107.604	107.6040 GHz	0.10±0.01	12.2±1.3		
U111.541	111.5410 GHz	0.07±0.01	12.7±2.0		

Note. — Table comments are the same as in Table 3.

Table 5.   DETECTED MOLECULES AND TRANSITIONS TOWARD IRAS 16293-2422

Species	Transition	ΔI (Jy beam^{-1})	Δv (km s^{-1})	ΔI (Jy beam^{-1})	Δv (km s^{-1})
		Fitted Data		Model Data	
		IRAS 16293-2422 A			
CH_3COOH	$10_{*,10} - 9_{*,9}\ E$	0.05±0.01	6.0±2.0	0.03	6
	$10_{*,10} - 9_{*,9}\ A$	0.05±0.01	6.0±2.0	0.05	6
$HCOOCH_3$	$9_{2,8} - 8_{2,7}\ E$	0.050±0.009	14.6±1.5	0.049	14.6
	$9_{2,8} - 8_{2,7}\ A$	0.050±0.008	14.6±1.5	0.049	14.6
U111.508	111.5080 GHz	0.05±0.01	5.0±2.0		
		IRAS 16293-2422 B			
CH_3COOH	$10_{*,10} - 9_{*,9}\ E$	<0.01			
	$10_{*,10} - 9_{*,9}\ A$	<0.01			
$HCOOCH_3$	$9_{2,8} - 8_{2,7}\ E$	0.063±0.005	5.5±0.5	0.059	5.5
	$9_{2,8} - 8_{2,7}\ A$	0.063±0.005	5.5±0.5	0.059	5.5
U111.510	111.5095 GHz	0.06±0.01	8.0±2.0		
U111.541	111.5410 GHz	0.06±0.01	5.0±1.0		

Table 6.   COLUMN DENSITIES OF THE OBSERVED MOLECULES

Species (cm^{-2})	G19.61-0.23	G29.96-0.02	I16293A	I16293B
CH_3COOH	$(2.0\pm1.0)\times10^{16}$	$< 9\times10^{14}$	$\sim1.6\times10^{15}$	$<6\times10^{14}$
$HCOOCH_3$	$(9.0\pm2.0)\times10^{16}$	$(4.0\pm1.0)\times10^{16}$	$(1.5\pm0.3)\times10^{16}$	$(6.0\pm1.0)\times10^{15}$
CH_3CH_2CN	$(6.0\pm3.0)\times10^{16}$	$(1.1\pm0.7)\times10^{16}$	$<6\times10^{13}$	$<3\times10^{14}$

Table 7.   COMPARISON OF CH_3COOH SOURCES

Species	Sgr B2(N-LMH)[a]	W51e2[b]	G34.3+0.15[c]	G19.61-0.23[d]	IRAS 16293 A[d]
N_{CH_3COOH} (cm^{-2})	$\sim7.3\times10^{15}$	$1.7\pm0.5\times10^{16}$	$(0.77\text{-}1.64)\times10^{15}$	$2.0\pm1.0\times10^{16}$	$\sim1.6\times10^{15}$
$N_{CH_3COOH}/N_{HCOOCH_3}$	$(4\text{-}7)\times10^{-2}$	$(1\text{-}6)\times10^{-2}$	$\sim3.3\times10^{-2}$	$2.2\pm0.1\times10^{-1}$	$1.0\pm0.1\times10^{-1}$

[a]Mehringer et al. (1997); T_r =200 K

[b]Remijan et al. (2002); T_r =201 K

[c]Remijan et al. (2003); T_r =70-185 K

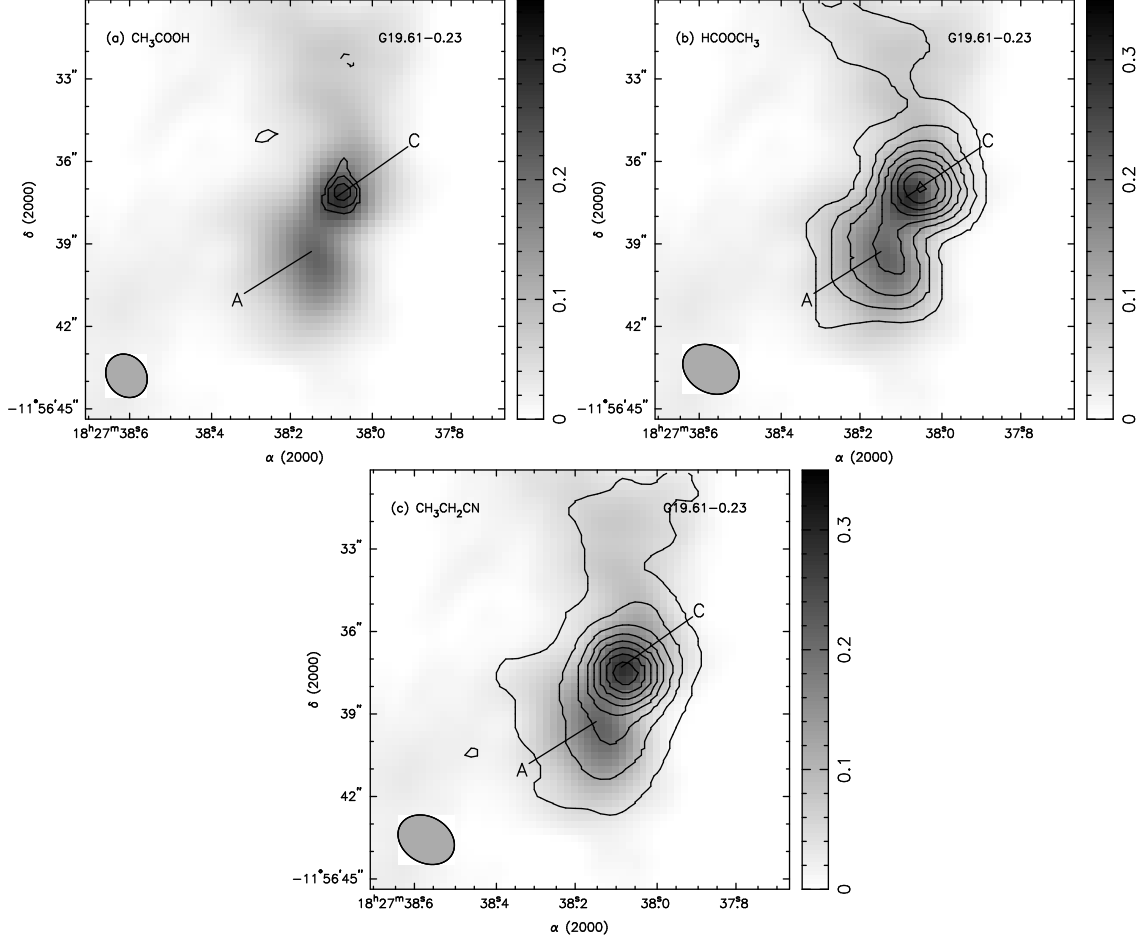[d]this work; T_r =161 K for G19 and T_r =62 K for I16293A

Fig. 1.— G19 maps. (a) CH$_3$COOH contours overlaid on the gray continuum map. The continuum emission maps shown were made from channels contained in the wideband windows which were free from line emission. The contour levels are -3, 3, 4 and 5 × σ = 24 mJy beam^{-1}. The gray scale unit is Jy beam^{-1}. The synthesized beam size is 1″65×1″42 (P.A.=46.3°), shown in the bottom left corner. The continuum beam size is 1″58×1″45 (P.A.=36.4°). In the continuum map, there are two main components, A and C. The CH$_3$COOH emission is mainly overlaid on component C. (b) HCOOCH$_3$ contours overlaid on the gray continuum map. The contour levels averaged over 3 channels are 3, 6, 9, 12, 15, 18, 21, 24, 27 and 30 × σ = 20 mJy beam^{-1}. The synthesized beam size is 2″16×1″67 (P.A.=59.6°). (c) CH$_3$CH$_2$CN contours overlaid on the gray continuum map. The contour levels averaged over 6 channels, are 3, 9, 15, 21, 27, 33, 39, 45, 51, 57 and 63 × σ = 18 mJy beam^{-1}. The synthesized beam size is 2″16×1″67 (P.A.=60.3°).
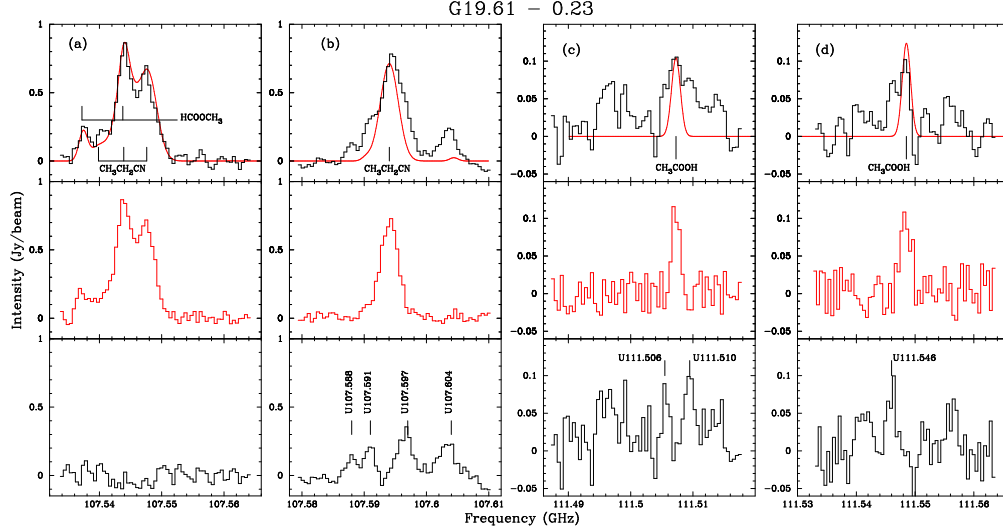
Fig. 2.— The observed spectra of G19.61-0.23. The first column (a) presents two HCOOCH$_3$ lines, $9_{2,8} - 8_{2,7}$ E and $9_{2,8} - 8_{2,7}$ A; and four CH$_3$CH$_2$CN lines, $12_{4,9} - 11_{4,8}$, $12_{4,8} - 11_{4,7}$, $12_{11,2} - 11_{11,1}$ and $12_{11,1} - 11_{11,0}$. The $12_{11,2} - 11_{11,1}$ and $12_{11,1} - 11_{11,0}$ lines are not spectrally resolved. The v$_{LSR}$ range is -15 to 69.4 km s^{-1}. The second column (b) contains only one known line, CH$_3$CH$_2$CN $12_{3,10} - 11_{3,9}$. The v$_{LSR}$ range is -3.4 to 81 km s^{-1}. The third column (c) contains the CH$_3$COOH $10_{*,10} - 9_{*,9}$ E line and the fourth column (d) contains the CH$_3$COOH $10_{*,10} - 9_{*,9}$ A line. The rest frequencies of the windows are 107.54375, 107.59404, 111.50727 and 111.54853 GHz, respectively. The v$_{LSR}$ ranges are 11.3 to 92.7 and -1.8 to 79.6 km s^{-1} for column (c) and (d), respectively. The first row presents the observed spectra (Hanning smoothed over 3 channels) overlaid on modeled spectral line data represented by Gaussians. The second row shows the modeled spectral line data from the first row convolved with the spectral resolution of the original observation and with random noise added to the spectrum. The value of the random noise is obtained with the line-free continuum spectrum in the windows. Finally, the third row shows the residuals from the modeled data in the second row subtracted from the observational data in the first row.
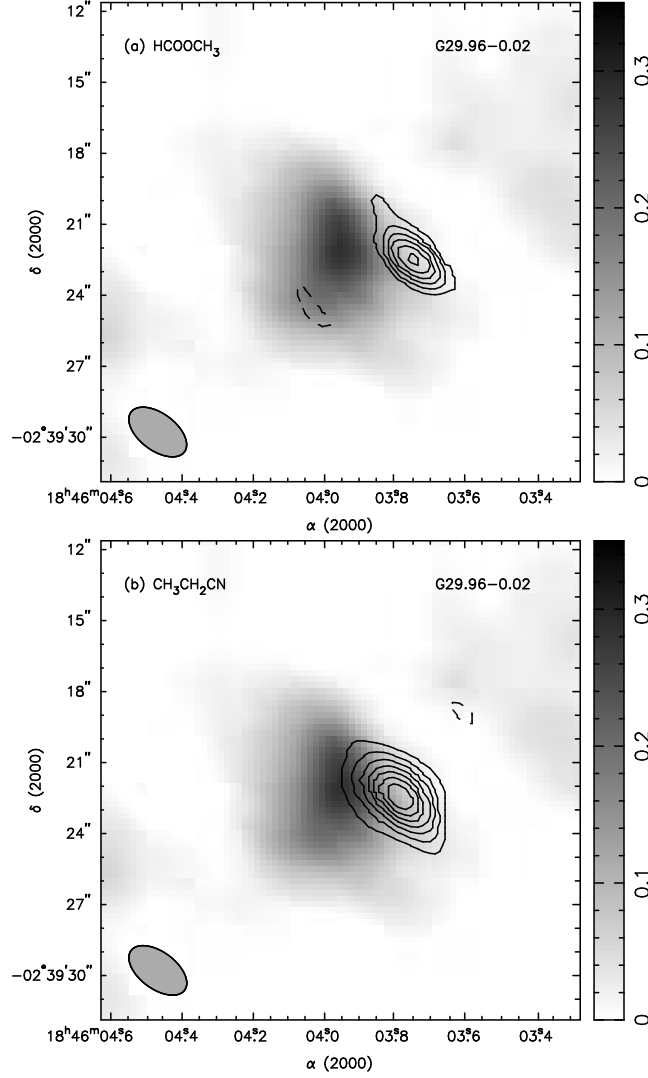
Fig. 3.— G29 maps. (a) HCOOCH$_3$ contours overlaid on the gray continuum map. The contour levels averaged over 3 channels are -3, 3, 4, 5, 6, 7 and 8 $\times$ σ = 21 mJy beam^{-1}. The synthesized beam size is 2$''$81$\times$1$''$56 (P.A.=53.2°), shown in the bottom left corner. (b) CH$_3$CH$_2$CN contours overlaid on the gray continuum map. The contour levels averaged over 6 channels, are -3, 3, 5, 7, 9, 11, 13 and 15 $\times$ σ = 16 mJy beam^{-1}. The synthesized beam size is 2$''$82$\times$1$''$56 (P.A.=53.5°).
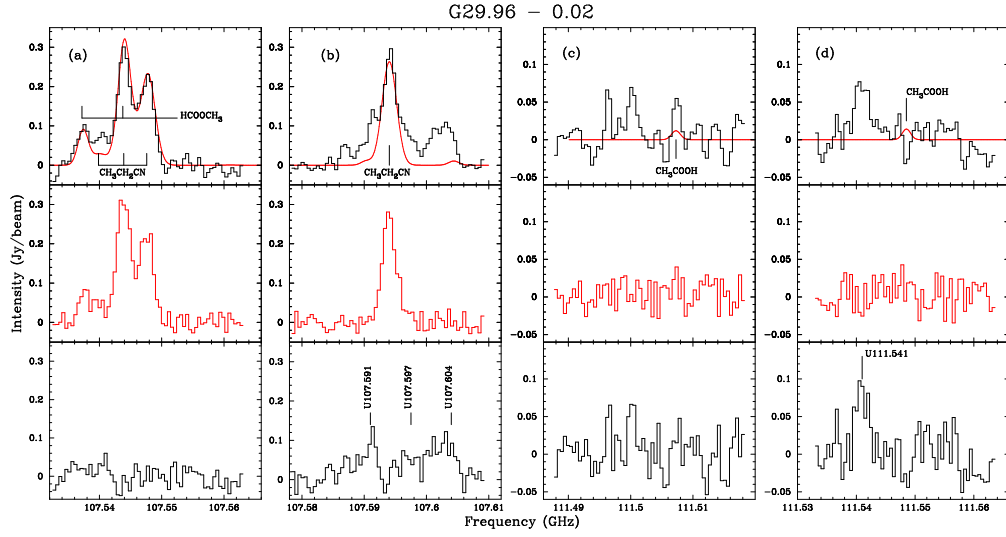
Fig. 4.— The observed spectra of G29.96-0.02. The arrangement of frequency and windows is the same as Figure 2. The v_{LSR} ranges are 44.6 to 129, 56.2 to 140.6, 68.8 to 150.2 and 55.7 to 137.1 km s^{-1}, respectively.
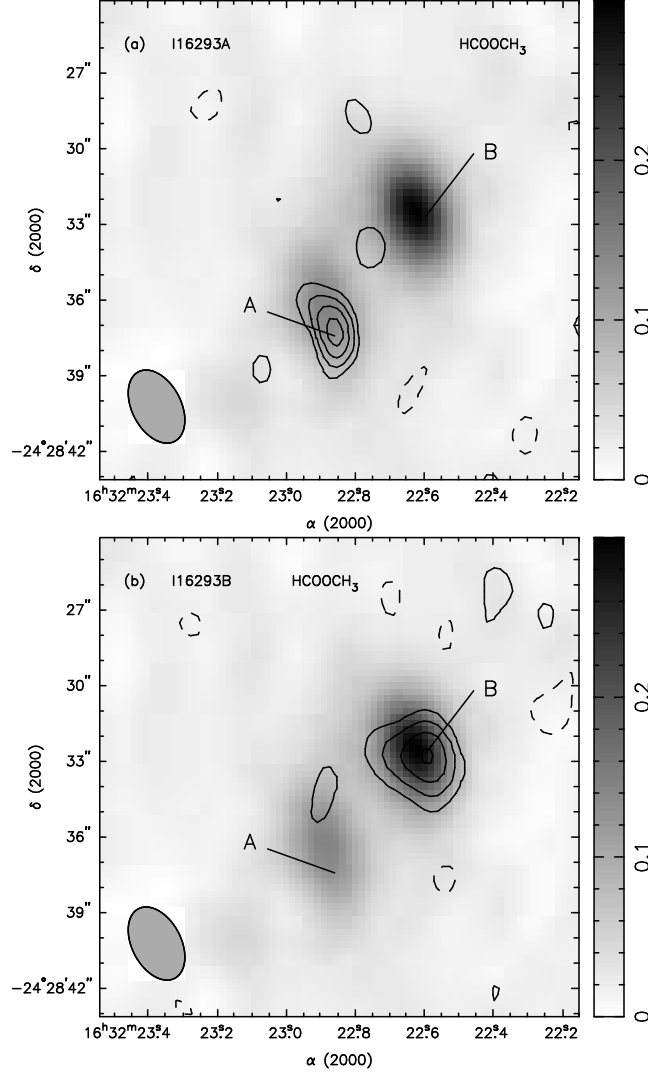
Fig. 5.— The HCOOCH$_3$ contour maps are made individually for I16293A and B (denoted as A and B on the maps) due to the different linewidths. The contours are overlaid on the gray continuum map of IRAS 16293-2422. (a) The contours located at I16293A are made with the $9_{2,8} - 8_{2,7}$ E line averaged over six channels. The contour levels are -2, 2, 3, 4 and 5 $\times$ $\sigma = 21$ mJy beam^{-1}. (b) The contours located at I16293B are made with one channel of the $9_{2,8} - 8_{2,7}$ E line. The contour levels are -2, 2, 3, 4 and 5 $\times$ $\sigma = 25$ mJy beam^{-1}.
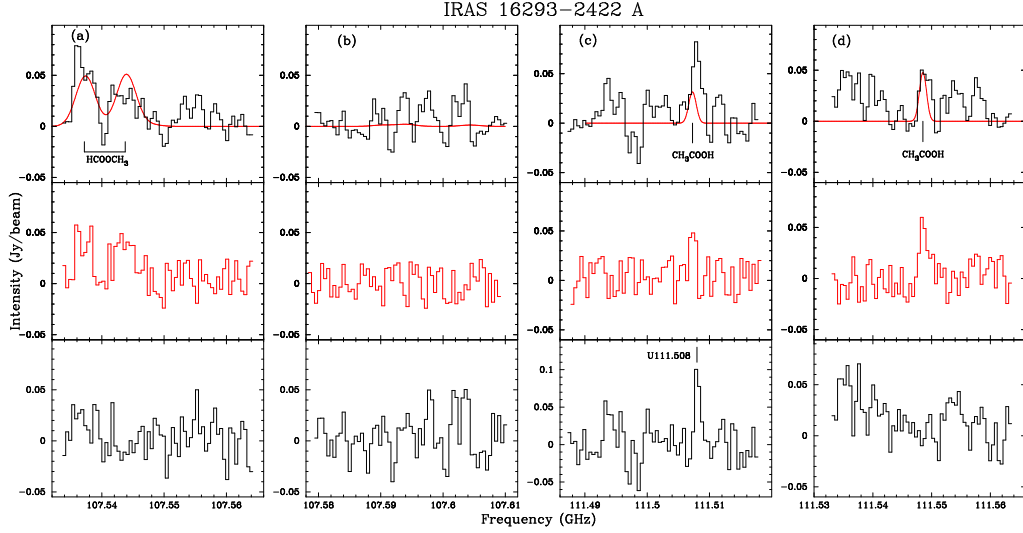
Fig. 6.— The observed spectra of I16293A. The arrangement of frequency and windows is the same as Figure 2. The column v_{LSR} ranges are 44.6 to 129, 56.2 to 140.6, 68.8 to 150.2 and 55.7 to 137.1 km s^{-1}, respectively.
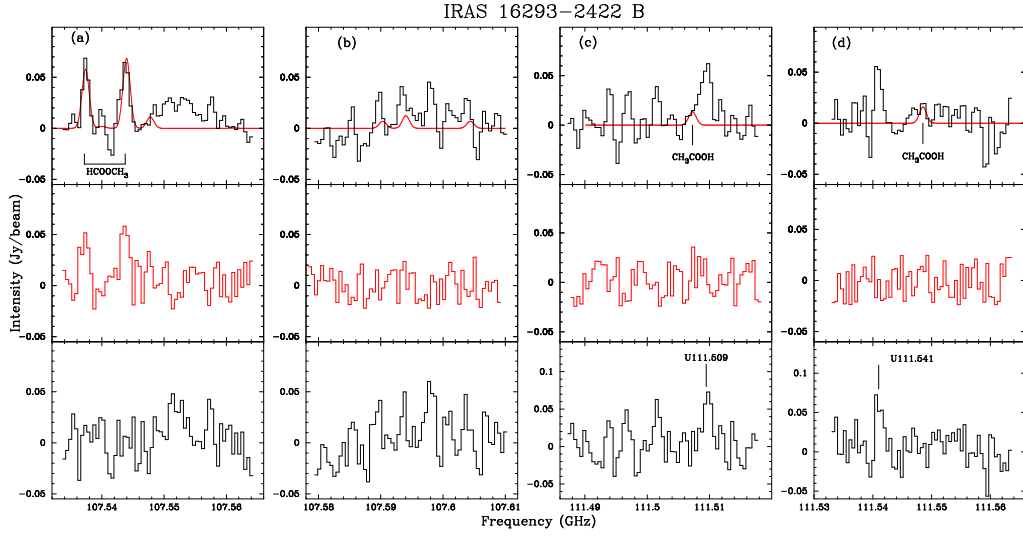

Fig. 7.— The observed spectra of I16293B. The arrangement of frequency and windows is the same as Figure 6. The column v_{LSR} ranges are -54.4 to 30, -42.7 to 41.6, -24.8 to 56.6 and -36.8 to 44.6 km s^{-1}, respectively.
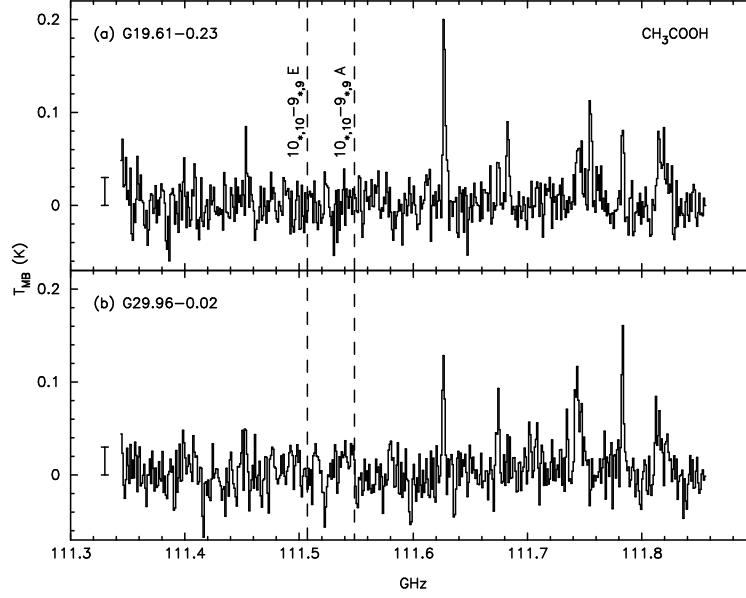
Fig. 8.— IRAM 30-m observations toward G19.61-0.23 and G29.96-0.02 (Fontani et al. 2007). The acetic acid lines are covered in this window at 111.50727 and 111.54853 GHz.